Intelligent Modeling and Decision Analytics

Journal homepage: www.imda.journal-publishing.org
ISSN: XXXX-XXXX

An Explainable Decision Analytics Framework for Multi Objective Design of Porous Al7075 B4C Functionally Graded Rotating Annular Disks

Hüseyin Fırat Kayiran[1,*]

[1] Presidency of the Agriculture and Rural Development Support Institution, Mersin Provincial Coordination Office, Mersin, Türkiye

ARTICLE INFO

Article history:
Received 7 June 2026
Received in revised form 19 August 2026
Accepted 17 September 2026
Available online 20 September 2026

Keywords:
Al7075-B4C; Porous functionally graded disk; Explainable artificial intelligence; Multi-objective optimization; Critical speed; Decision analytics

ABSTRACT

This study develops an explainable decision-analytics framework for the coupled thermo-centrifugal and vibrational design of porous functionally graded Al7075-B4C rotating annular disks. Radial ceramic gradation, temperature-dependent properties, and symmetric, inner-rich, outer-rich, and uniform porosity patterns are incorporated into nonlinear heat-conduction, axisymmetric thermoelastic, and prestressed vibration models. A Latin hypercube design comprising 240 successful governing-equation solutions is used to train and test four surrogate model families. Gaussian-process regression provides the highest mean test coefficient of determination ($R^2 = 0.968$) across eight reliable static and dynamic responses. KernelSHAP is applied directly to the selected Gaussian-process surrogate to quantify the global influence of the input variables. To prevent surrogate extrapolation from affecting the design decision, Pareto filtering and equal-weight TOPSIS are applied to the physics-based database rather than to unevaluated surrogate candidates. The resulting 43-member Pareto set yields a compromise design with $\Delta T = 56.48$ K, $\Omega = 1488.81$ rad/s, $n = 1.066$, $\varphi_0 = 0.014$, $r_i/r_o = 0.500$, $h/r_o = 0.037$, and a symmetric porosity pattern. Its synchronous critical speed is subsequently evaluated using only the governing physics solver, yielding 37,373.93 rad/s and a safety ratio of 25.10. The framework therefore combines interpretable surrogate screening with physics-based multi-objective selection and independent critical-speed verification.

1. Introduction

Rotating annular disks are fundamental load-carrying components in flywheels, turbine and compressor assemblies, braking systems, energy-storage units, and other high-speed machines. Their reliability is controlled by the coupled effects of centrifugal body force, non-uniform temperature, radial material variation, and vibration. These interactions can produce steep radial and circumferential stress gradients, alter the prestress-dependent modal characteristics, and reduce the separation between operating and critical speeds. Consequently, lightweight disk design requires the

* *Corresponding author.*
E-mail address: huseyinfiratkayiran@gmail.com

simultaneous evaluation of deformation, thermoelastic stress, natural frequency, travelling-wave behaviour, and critical-speed margin rather than isolated static or dynamic calculations [1–3].

Functionally graded materials (FGMs) mitigate abrupt interface effects by varying constituent fractions continuously in space. Recent reviews of functionally graded and architected systems have emphasized that composition, density, topology, and porosity can be tailored to obtain application-specific combinations of stiffness, mass, thermal transport, and structural performance [4]. For rotating annular disks, power-law radial gradation provides a compact means of controlling the metal–ceramic distribution, whereas a deliberately prescribed porosity field offers an additional lightweighting variable. Porosity, however, does not act as a uniformly beneficial design parameter: although it decreases mass, it also locally modifies elastic stiffness, heat conduction, thermal expansion, inertia, and the centrifugal prestress field. Its distribution must therefore be optimized together with the gradation index and disk geometry.

The present study considers an Al7075 matrix reinforced by boron carbide (B4C). Al7075 provides a low-density, high-specific-strength metallic base that is widely used in highly loaded engineering structures, while B4C combines low density with high elastic stiffness and comparatively low thermal expansion. Experimental research on Al7075/B4C/graphite composites has also confirmed the practical compatibility of the aluminium matrix with ceramic reinforcement and demonstrated that multiple responses can be balanced through a TOPSIS-based design procedure [5]. Recent work on AA7075–TiB2 composites further shows that high-strength aluminium matrix composites can be coupled with interpretable machine learning and Pareto analysis for process design [6]. These complementary characteristics make the Al7075–B4C pair attractive for radially graded rotating components in which mass, stiffness, and thermoelastic response must be balanced. The room-temperature constituent properties adopted as reference values are listed in Table 1; the Al7075 data follow the NASA materials handbook, while the representative B4C values are selected from the established boron-carbide property literature [7, 8].

High-fidelity thermo-mechanical and vibration simulations are indispensable for resolving these coupled effects, but repeated numerical analyses across a multi-dimensional design space can become computationally expensive. Jindal*et al.* [9] reviewed hybrid mechanistic and data-driven strategies and showed that machine-learning surrogates can reproduce complex numerical response maps at a fraction of the original computational cost when physical consistency and validation are retained. Raza *et al.* [10] similarly reported that artificial neural networks and other machine-learning approaches can support prediction and optimization in nonlinear heat-transfer systems. In manufacturing-oriented reviews, Fallahi *et al.* [11] and Mao *et al.* [12] organized machine-learning applications around forward property prediction, inverse parameter optimization, monitoring, and quality control, while stressing persistent limitations related to sparse data, generalization, and inconsistent validation. Wei *et al.* [13] further emphasized that interpretable and multi-objective AI can accelerate material design, but that reliability, heterogeneous data, and transparent validation remain central challenges.

Explainable artificial intelligence is particularly important when surrogate predictions are used to support an engineering design decision. Cesário*et al.* [14] integrated machine learning, Bayesian hyperparameter optimization, Shapley-value interpretation, and multi-objective metaheuristics for fibre-reinforced fused-filament process design; their study demonstrated how predictive accuracy, parameter influence, and Pareto trade-offs can be examined in a unified workflow. Szabó [15] likewise concluded that AI should operate as a physics-aware and validation-dependent accelerator of multiphysics design rather than as a substitute for mechanistic modelling. Anand *et al.* [16] combined ensemble learning, feature-importance analysis, and NSGA-II/MOEA-D optimization to reveal trade-offs among strength, durability, environmental impact, and cost. Lakshmaiya *et al.* [17]

embedded mechanistic relations into a neural-operator and evolutionary-optimization framework for metal-matrix composites, illustrating the value of physics-consistent surrogate optimization.

Recent studies by Kayiran provide direct methodological context for the present framework. Kayiran [18] combined physics-based thermoelastic analysis with machine learning to accelerate stress prediction in hybrid SiC-Ti6Al4V components, demonstrating the potential of surrogate models for computationally intensive thermo-mechanical design spaces. For rotating structures, Kayiran [19] developed an explainable physics-informed deep-learning framework for the thermoelastic analysis of Ti-6Al-4V disks, linking governing mechanics with interpretable data-driven prediction. Kayiran [20] also examined an axisymmetric layered cylinder under constant thermal loading and used artificial-intelligence-based validation to assess the thermoelastic solution. Together, these studies support the integration of axisymmetric field equations, physics-guided learning, and explainable validation adopted here, while the present work extends that direction to porous radial gradation, travelling-wave frequencies, critical-speed evaluation, and multi-objective decision analytics for Al7075-B4C annular disks.

Related studies also show the growing role of interpretable, data-driven decision support across materials and process engineering. Wang*et al.* [21] reviewed sensor-based and data-driven intelligence in mineral processing and highlighted the progression from prediction to optimization and adaptive control. Gürel *et al.* [22] surveyed AI, machine learning, physics-informed learning, digital twins, and surrogate modelling for coupled heat- and mass-transfer systems. Bayar *et al.* [4] identified AI-enabled property prediction and inverse design as important components of the process–structure–property framework for functionally graded structures. Xu *et al.* [23] framed sustainable materials design as a multi-objective problem linking composition, processing, structure, properties, and sustainability through heterogeneous data, while Delpisheh *et al.* [24] emphasized hybrid physics–ML models as a route to more accurate and interpretable prediction in porous systems. Pathak and Srivastava [25] described data-driven optimization and uncertainty-aware workflows as key enablers of next-generation smart-material design. Collectively, these studies establish the value of surrogate modelling, explainability, and multi-objective search, but they do not provide an integrated framework for the thermo-centrifugal stress, deformation, rotating-wave dynamics, and compromise selection of porous Al7075–B4C annular disks.

The broader decision-analytics literature also demonstrates that transparent normalization and compromise ranking can support engineering choices across heterogeneous performance criteria. Kara*et al.* [26] combined Fermatean fuzzy information with a double-normalized ALPAS framework for airport-service performance evaluation, while Hussain *et al.* [27] developed a multi-attribute decision framework for tram-service quality under a bipolar complex fuzzy environment. Although these studies address transportation services rather than structural materials, they illustrate the cross-domain role of auditable multi-criteria ranking. In the present work, uncertainty is not represented by fuzzy numbers; instead, equal-weight TOPSIS is deliberately restricted to alternatives already evaluated by the governing physics solver.

To address this gap, the present work develops an explainable decision-analytics framework that couples (i) radial power-law material gradation and controlled porosity distributions, (ii) nonlinear steady heat conduction and axisymmetric thermo-centrifugal analysis, (iii) prestress-dependent Kirchhoff-Love vibration modelling with forward and backward travelling waves, (iv) multi-response surrogate comparison, (v) KernelSHAP interpretation of the selected surrogate, and (vi) Pareto filtering followed by TOPSIS selection among physics-evaluated designs. Critical speed is retained as a governing-equation verification quantity and is not estimated or optimized by the surrogate. This separation prevents a weakly predicted root-search response from influencing the compromise design.

2. Methodology

2.1 Material Gradation and Thermoelastic Formulation

The effective properties are evaluated from the local constituent fractions and porosity. The room-temperature reference properties used for Al7075 and B4C are summarized in Table 1 [7, 8]. Temperature-dependent functions, when activated in the computational model, scale these reference values over the prescribed thermal range.

Table 1
Room-temperature reference properties of the Al7075 and B4C constituents [7, 8]

Material	E (GPa)	ν	ρ (kg/m³)	α (10^{-6} K^{-1})	k (W/mK)	c_p (J/kgK)
Al7075	71.7	0.33	2810	23.4	155	960
B4C	460	0.17	2520	4.5	30	950

The geometry, material gradation, porosity distribution, thermal boundary conditions, and rotational loading used in the formulation are summarized schematically in Figure 1. For the in-plane thermoelastic problem, both radial edges are traction-free, σr(ri) = σr(ro) = 0, while their temperatures are prescribed as Ti and To. For the transverse vibration problem, the inner edge is clamped and the outer edge is free. The illustrated ΔT = 200 K and symmetric porosity pattern correspond to the baseline case; the parametric study also considers ΔT = 40–300 K and symmetric, inner-rich, outer-rich, and uniform porosity distributions. The B4C fraction increases continuously from the Al7075-rich inner radius to the B4C-rich outer radius according to the radial power law.

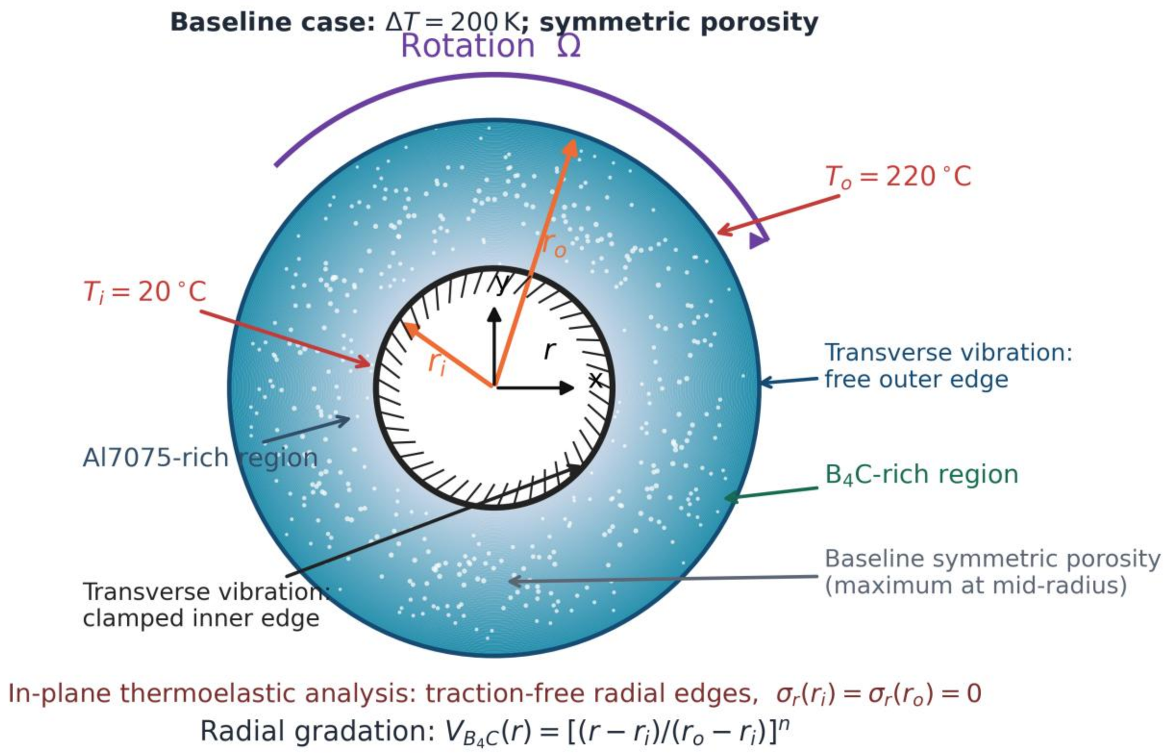

Fig. 1. Baseline configuration of the porous Al7075-B4C functionally graded rotating annular disk. The in-plane thermoelastic problem uses traction-free radial edges with prescribed temperatures, whereas the transverse vibration problem uses a clamped inner edge and a free outer edge. The illustrated symmetric porosity pattern and ΔT = 200 K correspond to the baseline case

The normalized radial coordinate is defined as

$$\xi = \frac{r - r_i}{r_o - r_i}, \qquad 0 \leq \xi \leq 1. \tag{1}$$

The B4C volume fraction is prescribed by the radial power law [2–4, 7, 8].

$$V_{B_4C}(r) = \left(\frac{r - r_i}{r_o - r_i}\right)^n = \xi^n. \tag{2}$$

The Al7075 volume fraction follows from

$$V_{Al7075}(r) = 1 - V_{B_4C}(r). \tag{3}$$

The local porosity field is expressed as

$$\phi(r) = \phi_0 f_p(\xi). \tag{4}$$

Representative porosity distributions are

$$f_p(\xi) = \begin{cases} 4\xi(1-\xi), & \text{symmetric,} \\ 1-\xi, & \text{inner-rich,} \\ \xi, & \text{outer-rich,} \\ 1, & \text{uniform.} \end{cases} \tag{5}$$

For a generic material property $P \in \{E, \nu, \rho, \alpha, k\}$, the porous effective property is

$$P_{eff}(r,T) = \left[P_{Al7075}(T)V_{Al7075}(r) + P_{B_4C}(T)V_{B_4C}(r)\right][1 - \lambda_P \phi(r)]. \tag{6}$$

The steady axisymmetric heat-conduction equation is (2, 3, 10).

$$\frac{1}{r}\frac{d}{dr}\left[r k_{eff}(r,T)\frac{dT}{dr}\right] = 0. \tag{7}$$

The thermal boundary conditions are

$$T(r_i) = T_i, \qquad T(r_o) = T_o, \qquad \Delta T = T_o - T_i. \tag{8}$$

The radial equilibrium equation including centrifugal body force is [1–3, 18–20].

$$\frac{d\sigma_r}{dr} + \frac{\sigma_r - \sigma_\theta}{r} + \rho_{eff}(r,T)\Omega^2 r = 0. \tag{9}$$

The axisymmetric strain-displacement relations are

$$\varepsilon_r = \frac{du}{dr}, \qquad \varepsilon_\theta = \frac{u}{r}. \tag{10}$$

Under plane-stress conditions, the thermoelastic constitutive equations are [1–3, 18–20].

$$\begin{bmatrix}\sigma_r \\ \sigma_\theta\end{bmatrix} = \frac{E_{eff}}{1-\nu_{eff}^2}\begin{bmatrix}1 & \nu_{eff} \\ \nu_{eff} & 1\end{bmatrix}\left(\begin{bmatrix}\varepsilon_r \\ \varepsilon_\theta\end{bmatrix} - \alpha_{eff}\left(T - T_{ref}\right)\begin{bmatrix}1 \\ 1\end{bmatrix}\right). \tag{11}$$

For traction-free radial edges,

$$\sigma_r(r_i) = 0, \qquad \sigma_r(r_o) = 0. \tag{12}$$

The equivalent plane-stress von Mises stress is

$$\sigma_{vm} = \sqrt{\sigma_r^2 - \sigma_r\sigma_\theta + \sigma_\theta^2}. \tag{13}$$

The peak thermo-mechanical response measures used in surrogate modelling are

$$\sigma_{r,max} = \max_{r_i \leq r \leq r_o} |\sigma_r(r)|, \qquad \sigma_{\theta,max} = \max_{r_i \leq r \leq r_o} |\sigma_\theta(r)|, \qquad u_{r,max} = \max_{r_i \leq r \leq r_o} |u(r)|. \tag{14}$$

The radial and circumferential membrane-force resultants are

$$N_r(r) = h\sigma_r(r), \qquad N_\theta(r) = h\sigma_\theta(r). \tag{15}$$

The spatially varying flexural rigidity is

$$D(r,T) = \frac{E_{eff}(r,T)h^3}{12\left[1-\nu_{eff}^2(r,T)\right]}. \tag{16}$$

2.2 Vibration and Critical Speed Formulation

For circumferential wave number m, the transverse displacement is represented as

$$w(r,\theta,t) = W(r)\cos(m\theta)e^{i\omega t}. \tag{17}$$

The admissible radial displacement function is expanded as

$$W(r) = \sum_{j=1}^{N_b} a_j\,\psi_j(\xi), \qquad \psi_j(\xi) = \xi^{j+1}. \tag{18}$$

The selected basis satisfies the clamped inner-edge conditions

$$W(r_i) = 0, \qquad \left.\frac{dW}{dr}\right|_{r=r_i} = 0. \tag{19}$$

The generalized eigenvalue problem including geometric stiffness is [1, 2, 28, 29].

$$\left(\mathrm{K}_b + \mathrm{K}_g - \omega^2\mathrm{M}\right)\mathrm{a} = 0. \tag{20}$$

The bending-stiffness matrix is obtained from

$$K_{b,ij} = \pi\int_{r_i}^{r_o} D\left[\kappa_{r,i}\kappa_{r,j} + \kappa_{\theta,i}\kappa_{\theta,j} + \nu\left(\kappa_{r,i}\kappa_{\theta,j} + \kappa_{\theta,i}\kappa_{r,j}\right) + \frac{1-\nu}{2}\kappa_{s,i}\kappa_{s,j}\right] r\,dr. \tag{21}$$

The geometric-stiffness matrix associated with the prestress field is

$$K_{g,ij} = \pi\int_{r_i}^{r_o}\left[N_r\frac{d\psi_i}{dr}\frac{d\psi_j}{dr} + N_\theta\frac{m^2}{r^2}\psi_i\psi_j\right] r\,dr. \tag{22}$$

The mass matrix is

$$M_{ij} = \pi\int_{r_i}^{r_o}\rho_{eff}\,(r,T)h\psi_i\psi_j r\,dr. \tag{23}$$

The rotating-frame natural frequencies follow from [28, 29].

$$f_j = \frac{\omega_j}{2\pi}. \tag{24}$$

The forward and backward travelling-wave frequencies are [28, 29].

$$f_{F,j} = \frac{\omega_j + m\Omega}{2\pi}, \qquad f_{B,j} = \frac{|\omega_j - m\Omega|}{2\pi}. \tag{25}$$

The synchronous critical-speed condition is

$$\omega_j(\Omega_{cr}) = m\Omega_{cr}. \tag{26}$$

2.3 Machine Learning and Decision Analytics

The computational database was generated by Latin hypercube sampling with a fixed seed of 318. All 240 sampled designs converged and were retained. The continuous ranges were Delta T = 40-300 K, Omega = 75-1500 rad/s, n = 0.15-8.0, phi0 = 0-0.12, ri/ro = 0.30-0.70, and h/ro = 0.015-0.055. Circumferential wave numbers m = 3, 4, 5, and 6 and four porosity patterns were balanced across the database. An 80/20 train-test split with the same seed was used. Multilayer perceptron, random forest, gradient boosting, and Gaussian-process regression were compared. The Gaussian process used standardized inputs, a constant-times-Matern kernel (nu = 2.5), a white-noise term, normalized targets, and one optimizer restart.

KernelSHAP was evaluated directly on the selected Gaussian-process model using 20 k-means background points and the 48 held-out test designs. Mean absolute SHAP values were normalized separately for each response and then averaged to obtain global importance. Pareto dominance and TOPSIS were applied only to the 240 physics-evaluated designs. Equal weights were assigned to maximum radial, circumferential, and von Mises stresses, maximum radial displacement, mass, and fundamental frequency; the first five quantities were treated as costs and frequency as a benefit. Critical speed was excluded from surrogate training and TOPSIS, and was computed with the governing-equation solver only after selecting the compromise design.

The surrogate relationship between the design variables and reliable structural responses is written as [9, 11–20].

$$\hat{\mathbf{y}} = \mathcal{M}(\mathbf{x}), \qquad \mathbf{x} = [\Delta T, \Omega, n, \phi_0, r_i/r_o, h/r_o, m]^T. \tag{27}$$

The surrogate output vector combines the eight static and dynamic quantities used for prediction:

$$\mathbf{y} = \left[\sigma_{r,max}, \sigma_{\theta,max}, \sigma_{vm,max}, u_{r,max}, M_d, f_1, f_{F,1}, f_{B,1}\right]^T. \tag{28}$$

The coefficient of determination is [11, 12, 14–17].

$$R^2 = 1 - \frac{\sum_{i=1}^{N}(y_i - \hat{y}_i)^2}{\sum_{i=1}^{N}(y_i - \bar{y})^2}. \tag{29}$$

The root-mean-square error is

$$RMSE = \sqrt{\frac{1}{N}\sum_{i=1}^{N}(y_i - \hat{y}_i)^2}. \tag{30}$$

The mean absolute error is

$$MAE = \frac{1}{N}\sum_{i=1}^{N}|y_i - \hat{y}_i|. \tag{31}$$

The physics-based multi-objective design problem is defined as [14–17].

$$\min_{\mathbf{x}} \mathbf{F}(\mathbf{x}) = \left[\sigma_{r,max}, \sigma_{\theta,max}, \sigma_{vm,max}, u_{r,max}, M_d, -f_1\right]^T. \tag{32}$$

For TOPSIS, the normalized decision matrix is [5, 30, 31].

$$r_{ij} = \frac{x_{ij}}{\sqrt{\sum_{i=1}^{N} x_{ij}^2}}. \tag{33}$$

The weighted normalized matrix is

$$v_{ij} = w_j r_{ij}, \qquad \sum_{j=1}^{J} w_j = 1. \tag{34}$$

The distances from the positive and negative ideal solutions are

$$S_i^+ = \sqrt{\sum_{j=1}^{J}\left(v_{ij} - v_j^+\right)^2}, \qquad S_i^- = \sqrt{\sum_{j=1}^{J}\left(v_{ij} - v_j^-\right)^2}. \tag{35}$$

The TOPSIS closeness coefficient is

$$C_i = \frac{S_i^-}{S_i^+ + S_i^-}. \tag{36}$$

3. Results and Discussion

3.1 Baseline Thermo-Mechanical Response

Figure 2 presents the radial fields obtained for the baseline disk (r_i = 50 mm, r_o = 90 mm, h = 3 mm, Omega = 500 rad/s, Delta T = 200 K, n = 1.0, and phi_0 = 0.04) with a symmetric porosity distribution. As shown in Figure 2(a), the temperature increases monotonically from 20 degrees C at the inner boundary to 220 degrees C at the outer boundary. The nonlinear profile reflects the radial variation of effective thermal conductivity induced by the Al7075-B4C gradation and porosity field.

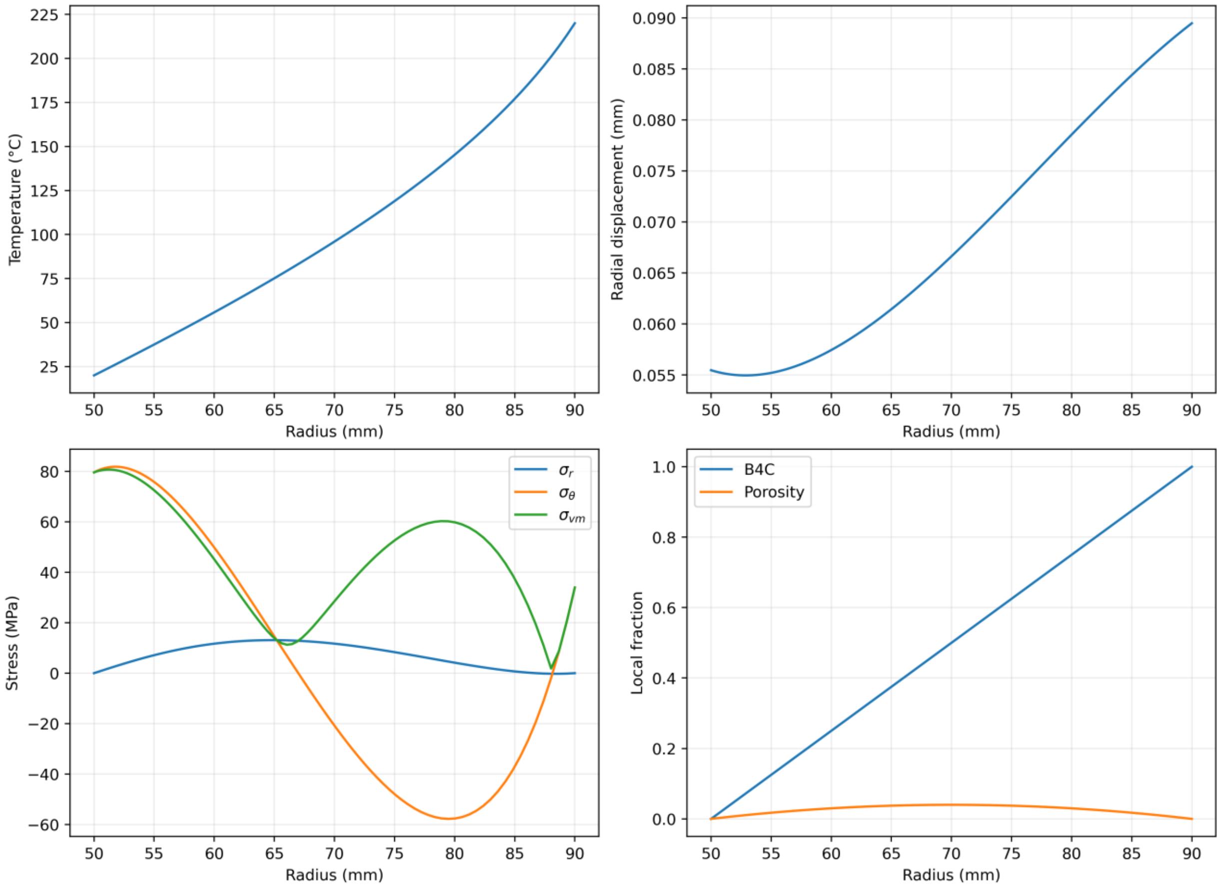

Fig. 2. Baseline radial response of the porous Al7075-B4C functionally graded annular disk: (a) temperature, (b) radial displacement, (c) radial, circumferential, and von Mises stresses, and (d) B4C volume fraction and local porosity

As can be seen in Figure 2(b), the radial displacement initially decreases slightly and then rises toward the outer edge, reaching a maximum value of 0.0895 mm. Figure 2(c) shows that the radial stress satisfies the traction-free boundary conditions at both edges and reaches an interior maximum of 13.08 MPa near r = 64.8 mm. The circumferential stress is tensile close to the inner radius, with a peak value of 81.79 MPa, becomes compressive through the thermally affected outer part of the disk, and reaches approximately -57.74 MPa near r = 79.5 mm. The von Mises stress follows the dominant circumferential-stress contribution and attains a maximum of 80.66 MPa near the inner region. This sign change and redistribution indicate that the response cannot be represented adequately by centrifugal loading alone; thermal expansion mismatch and radial gradation are essential to the resulting stress field.

Figure 2(d) confirms the intended linear increase in B4C fraction from the Al7075-rich inner edge to the B4C-rich outer edge for n = 1.0. The symmetric porosity field vanishes at both boundaries and reaches its prescribed maximum of approximately 0.04 near the mid-radius. The coincidence of the porosity maximum with the transition region modifies the local stiffness and thermal transport without introducing a discontinuous material interface.

3.2 Surrogate Prediction Performance

The four surrogate candidates were compared using the 48-design held-out test set. Gaussian-process regression achieved the highest mean test R2 of 0.968 across the eight retained outputs and was selected for parity assessment and SHAP interpretation. Figure 3 compares its predictions with the governing-equation solutions; the dashed 45-degree line denotes ideal agreement.

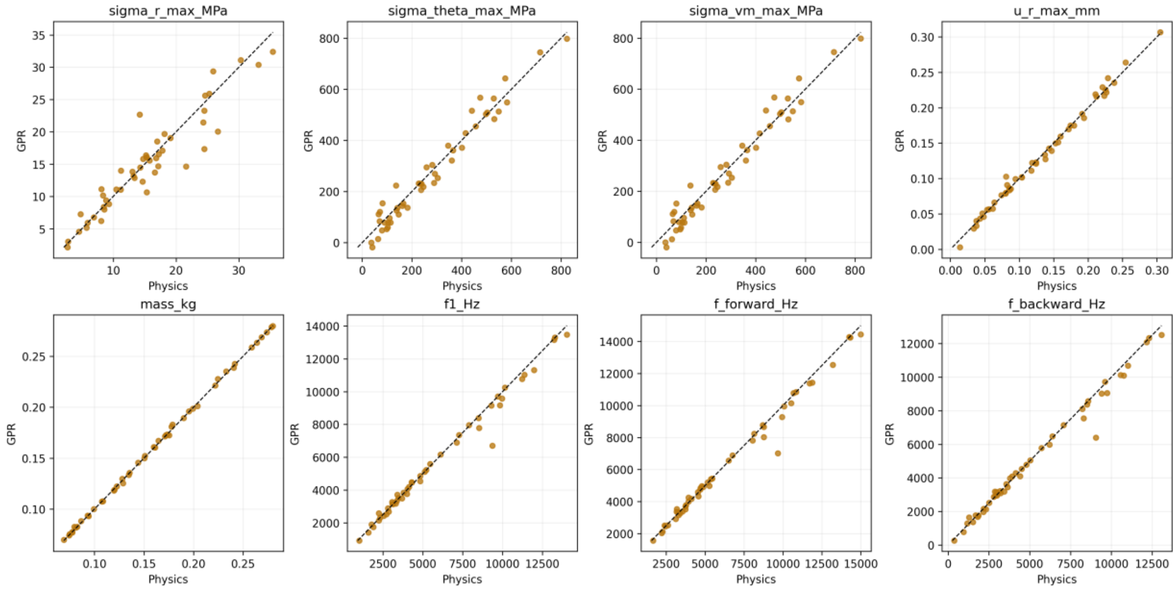

Fig. 3. Governing-equation versus Gaussian-process predictions for maximum radial, circumferential, and von Mises stresses, radial displacement, mass, fundamental frequency, and forward and backward travelling-wave frequencies

As shown in Figure 3, the Gaussian process reproduces displacement, mass, and vibration responses particularly well. The test R2 values are 0.882 for maximum radial stress, 0.958 for maximum circumferential stress, 0.958 for maximum von Mises stress, 0.993 for maximum radial displacement, 0.999 for mass, 0.983 for fundamental frequency, 0.984 for forward frequency, and 0.983 for backward frequency. The corresponding mean R2 of 0.968 supports surrogate use for interpolation and sensitivity interpretation. Because the radial-stress response is the least accurate and surrogate extrapolation can still create nonphysical optima, the final Pareto and TOPSIS calculations are restricted to designs already evaluated by the governing solver.

Synchronous critical speed is intentionally excluded from surrogate training and multi-objective ranking. It is obtained from the nonlinear synchronous root condition only for the final physics-selected design. This conservative separation avoids carrying uncertainty from a difficult root-search response into TOPSIS.

3.3 Gaussian-Process SHAP Interpretation

Figure 4 reports the global KernelSHAP importance calculated directly for the selected Gaussian-process surrogate. The circumferential wave number, porosity pattern, and thickness ratio contribute 30.66%, 28.30%, and 24.94% of the averaged normalized absolute SHAP magnitude, respectively. The gradation index and rotational speed contribute approximately 7.89% each. These values are global associations within the sampled design domain and should not be interpreted as causal effects.

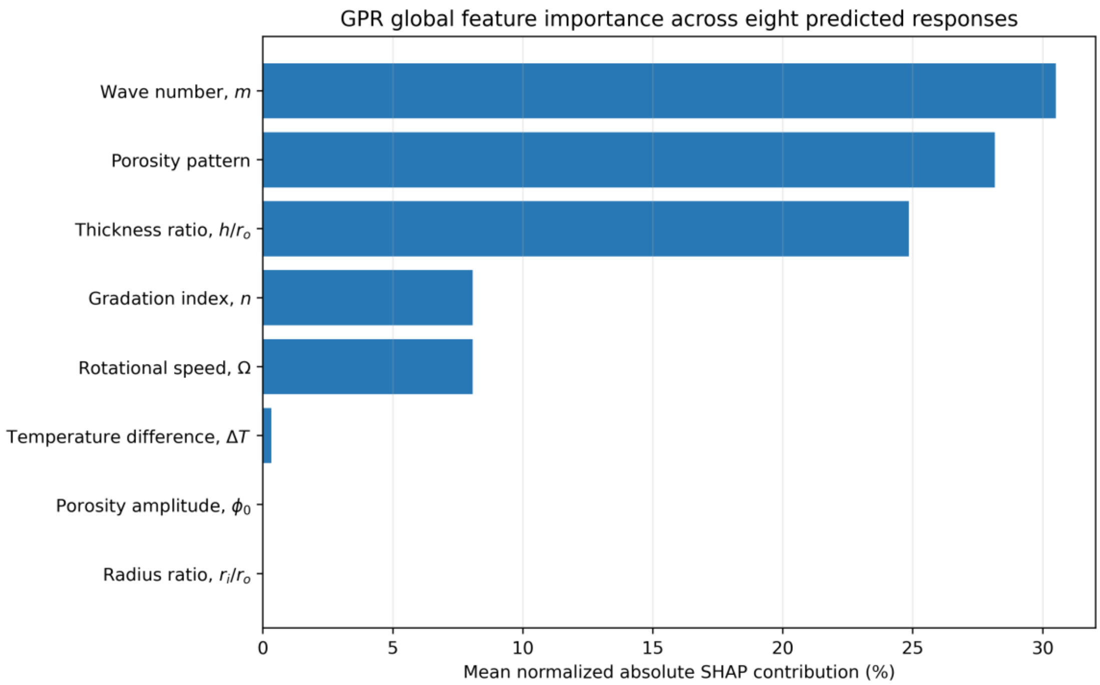

Fig. 4. Global KernelSHAP feature importance for the selected Gaussian-process surrogate, averaged across the eight retained response variables

3.4 Physics-Based Pareto and TOPSIS Selection

Pareto filtering of the 240 governing-equation solutions produced 43 nondominated designs. Figure 5 shows their mass-von Mises stress projection, coloured by fundamental frequency. TOPSIS was evaluated with equal weights over the six stated criteria. The starred point is the highest-ranked compromise and is an evaluated physics solution rather than an unverified surrogate optimum.

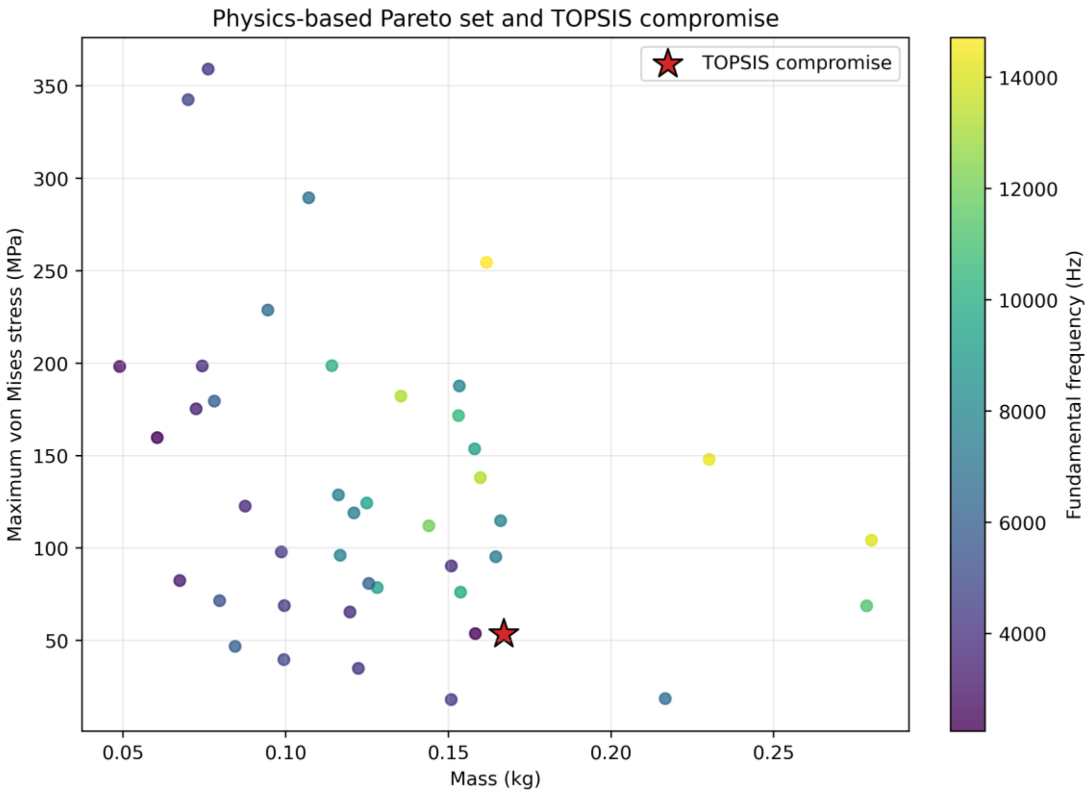

Fig. 5. Physics-based Pareto set and equal-weight TOPSIS compromise design

Table 2
Five highest-ranked physics-based TOPSIS designs

1	56.48	1488.81	1.066	0.014	0.500	0.037	Symmetric	0.788
2	140.62	660.57	0.473	0.021	0.697	0.042	Outer-rich	0.744
3	107.93	664.16	0.757	0.116	0.515	0.020	Outer-rich	0.744
4	82.30	1368.35	1.351	0.033	0.553	0.019	Outer-rich	0.743
5	40.86	279.35	1.047	0.005	0.445	0.031	Inner-rich	0.743

The selected design has Delta T = 56.48 K, Omega = 1488.81 rad/s, n = 1.066, phi0 = 0.014, ri/ro = 0.500, h/ro = 0.037, m = 6, and symmetric porosity. Its governing-equation responses are sigma_r,max = 4.94 MPa, sigma_theta,max = sigma_vm,max = 53.62 MPa, ur,max = 0.0336 mm, mass = 0.1670 kg, and f1 = 10811.46 Hz. The independently evaluated synchronous critical speed is 37373.93 rad/s, giving a margin of 35885.12 rad/s and an Omega_cr/Omega safety ratio of 25.10. Accordingly, no surrogate-predicted critical-speed value enters the selection.

4. Conclusions

The coupled governing-equation model resolves the nonlinear temperature, displacement, and stress fields of the porous Al7075-B4C disk while satisfying traction-free in-plane radial boundaries and separate clamped-free transverse vibration conditions. A 240-design database provided complete converged solutions. Gaussian-process regression achieved a mean test R2 of 0.968 across eight retained responses, and KernelSHAP identified wave number, porosity pattern, and thickness ratio as the dominant global inputs. To avoid surrogate-extrapolation risk, Pareto filtering and TOPSIS were performed directly on the physics database, producing 43 nondominated designs. The selected compromise attained a TOPSIS coefficient of 0.788 and was already a governing-equation solution. Its critical speed was evaluated separately by the physics solver, with Omega_cr/Omega = 25.10. The resulting workflow supports interpretable surrogate screening while reserving design selection and critical-speed verification for physics-evaluated configurations.

Acknowledgement

This research was not funded by any grant.

Conflicts of Interest

The author declares no conflicts of interest.

References

[1] Bahaloo, H., & Nayeb-Hashemi, H. (2022). Stress analysis and thermoelastic instability of an annular functionally graded rotating disk. Journal of Thermal Stresses, 45(1), 1-11. https://doi.org/10.1080/01495739.2021.2013748

[2] Allam, M. N., Tantawy, R., & Zenkour, A. M. (2018). Thermoelastic stresses in functionally graded rotating annular disks with variable thickness. *Journal of Theoretical and Applied Mechanics*, *56*(4), 1029-1041. https://doi.org/10.15632/jtam-pl.56.4.1029

[3] Callioglu, H., Bektas, N. B., & Sayer, M. (2011). Stress analysis of functionally graded rotating discs: Analytical and numerical solutions. Acta Mechanica Sinica, 27(6), 950–955. https://doi.org/10.1007/s10409-011-0499-8

[4] Bayar, A., Altun, F., Sarac, A. E., Ateiwi, S., Alasahin, S. N., & Asmatulu, E. (2026). Additive manufacturing of functionally graded lattice structures: Process–structure–property relationships, design strategies, and future perspectives. Journal of Manufacturing and Materials Processing, 10(8), 267. https://doi.org/10.3390/jmmp10080267

[5] Kolli, M., Ram Prasad, A. V. S., & Naresh, D. S. (2021). Multi-objective optimization of AAJM process parameters for cutting of B4C/Gr particles reinforced Al 7075 composites using RSM–TOPSIS approach. SN Applied Sciences, 3(7), 711. https://doi.org/10.1007/s42452-021-04699-x

[6] Sakthimurugan, D., Barathkumar, M. D., Madesh, R., Vignesh, M., & Sathishkumar, M. (2026). Optimization and Machine Learning assisted Insight Analysis of Biosilica-Mixed EDM of AA7075–TiB 2 Metal Matrix Composites. *IEEE Access*. https://doi.org/10.1109/ACCESS.2026.3694710

[7] Sessler, J. G., & Weiss, V. (1966). Materials data handbook: Aluminum alloy 7075. NASA Marshall Space Flight Center, NASA-CR-116487.

[8] Thévenot, F. (1990). Boron carbide—A comprehensive review. Journal of the European Ceramic Society, 6(4), 205–225. https://doi.org/10.1016/0955-2219(90)90048-K

[9] Jindal, C., Kumar, R., Kumar, R., *et al.* (2026). Artificial intelligence, machine learning, and deep learning for solid particle erosion: Computational modeling, predictive optimization, and research roadmap. Archives of Computational Methods in Engineering. https://doi.org/10.1007/s11831-026-10581-z

[10] Raza, M., Faiz, M., Hassan, W. U. I., *et al.* (2025). AI-powered optimization and numerical techniques for nanofluid heat transfer systems—a review. Multiscale and Multidisciplinary Modeling, Experiments and Design, 8(7), 316. https://doi.org/10.1007/s41939-025-00891-3

[11] Fallahi, H., Baqershahi, M. H., Moshayedi, H., Ryan, M., & Ghafoori, E. (2026). Machine learning in directed energy deposition: A systematic literature review. Journal of Manufacturing Processes, 175, 76–108. https://doi.org/10.1016/j.jmapro.2026.07.081

[12] Mao, Y., Jiang, D., Vladimir, U., Jing, Z., & Wang, L. (2025). Machine learning-driven additive manufacturing of biomedical metals: A review of forward prediction, inverse optimization, and quality control. Engineering Science in Additive Manufacturing, 1(4), 025440031. https://doi.org/10.36922/ESAM025440031

[13] Wei, D., Wang, Z., Lin, H., Yin, X. P., & Wang, Y. (2026). Research progress in artificial intelligence-assisted preparation of high-quality biomaterials. ACS Omega, 11, 10971–11000. https://doi.org/10.1021/acsomega.5c09392

[14] Cesário, M. C., Pereira, M. C., de Souza, L. E. B., *et al.* (2026). Explainable machine learning and multi-objective optimization for PET-CF15 fused filament fabrication process design. The International Journal of Advanced Manufacturing Technology, 143(9-10), 5377–5397. https://doi.org/10.1007/s00170-026-17838-8

[15] Szabó, L. (2026). AI-driven electrical machine design: From surrogate-assisted optimization to trustworthy, manufacturable, and sustainable design workflows. Designs, 10(4), 76. https://doi.org/10.3390/designs10040076

[16] Anand, P., Singh, S. D., Pratap, S., Asaithambi, P., & Bidira, F. (2026). Data-driven optimisation of sustainable high-performance concrete incorporating SCMs, biomass ash, and graphene nanoplatelets. Scientific Reports, 16(1), 10657. https://doi.org/10.1038/s41598-026-45032-z

[17] Lakshmaiya, N., Chakrapani, G., Sagar, V., *et al.* (2026). Mechanistic neural operator framework for multi-objective optimization of Ti-6Al-4V metal matrix composites. Scientific Reports, 16(1), 18771. https://doi.org/10.1038/s41598-026-49745-z

[18] Kayiran, H. F. (2026). Sustainable engineering design: Accelerating thermoelastic stress prediction in hybrid SiC-Ti6Al4V components via machine learning. International Journal of Sustainable Development Goals, 2, 655-667. https://doi.org/10.59543/dbs4d790

[19] Kayiran, H. F. (2026). Explainable physics-informed deep learning framework for thermoelastic analysis of rotating Ti-6Al-4V disks. Applied Expert Systems and Knowledge Management, 1, 1-15. https://doi.org/10.59543/qhn3ek50

[20] Kayiran, H. F. (2026). Thermo-elastic analysis of an axisymmetric layered cylinder under constant thermal loading with artificial intelligence-based validation. Intelligent Systems Research and Applications Journal, 2, 54-67. https://doi.org/10.59543/0x8ky937

[21] Wang, X., Su, B., Shao, A., Fu, Y., Liu, J., Song, Z., ... & Yin, W. (2026). Data-driven artificial intelligence in mineral processing: From sensor technology, intelligent algorithms to Genetic Mineral Processing Engineering. *International Journal of Minerals, Metallurgy and Materials*.

[22] Gürel, A. E., Yıldız, G., & Bakır, H. (2026). Artificial intelligence and machine learning applications in drying systems: A comprehensive review. Drying Technology, 1-26. https://doi.org/10.1080/07373937.2026.2726458

[23] Xu, T., Wei, T., Ge, Y., *et al.* (2026). Sustainable materials design with multi-modal artificial intelligence. Advanced Science, e24273. https://doi.org/10.1002/advs.202524273

[24] Delpisheh, M., Ebrahimpour, B., Fattahi, A., *et al.* (2024). Leveraging machine learning in porous media. Journal of Materials Chemistry A, 12(32), 20717-20782. https://doi.org/10.1039/D4TA00251B

[25] Pathak, P., & Srivastava, S. (2026). Smart material design: Integrating data-driven optimization and complexity analysis for next-generation materials. In Smart Materials Engineering (pp. 41–63). Springer. https://doi.org/10.1007/978-3-032-09540-4_3

[26] Kara, K., Yalcin, G. C., Ozekenci, E. K., & Moslem, S. (2026). Advancing hybrid Fermatean fuzzy and double-normalized ALPAS framework for airport service performance evaluation. Research in Transportation Business & Management, 69, 101871. https://doi.org/10.1016/j.rtbm.2026.101871

[27] Hussain, A., Moslem, S., Senapati, T., & Esztergar-Kiss, D. (2026). Ameliorating tram service quality using a multi-attribute decision-making framework in a bipolar complex fuzzy environment. Intelligent Systems with Applications, 31, 200721. https://doi.org/10.1016/j.iswa.2026.200721

[28] Jalali, M. H., Shahriari, B., Zargar, O., Baghani, M., & Baniassadi, M. (2018). Free vibration analysis of rotating functionally graded annular disc of variable thickness using generalized differential quadrature method. *Scientia Iranica. Transaction B, Mechanical Engineering*, *25*(2), 728-740. https://doi.org/10.24200/sci.2017.4325

[29] Callioglu, H., & Muftu, S. (2025). Damped vibration responses of functionally graded rotating discs with variable geometry and modeling with deep neural networks. *Journal of Vibration Engineering & Technologies*, *13*(5), 331. https://doi.org/10.1007/s42417-025-01900-y

[30] Hwang, C. L., & Yoon, K. (1981). Multiple attribute decision making: Methods and applications. Springer. https://doi.org/10.1007/978-3-642-48318-9

[31] Kulkarni, A. J. (2025). Optimization methods in traditional machining processes. In Optimization Methods in Manufacturing Processes (pp. 67–135). Springer. https://doi.org/10.1007/978-981-96-5257-0_2